PAPER

The shell effect on the room temperature photoluminescence from ZnO/MgO core/shell nanowires: exciton–phonon coupling and strain

To cite this article: N C Vega *et al* 2017 *Nanotechnology* **28** 275702

View the article online for updates and enhancements.

Related content

- Enhanced optical properties and (Zn, Mg) interdiffusion in vapour transport grown ZnO/MgO core/shell nanowires
G Grinblat, L J Borrero-González, L A O Nunes et al.
- ZnO nanowire co-growth on SiO2 and C by carbothermal reduction and vapour advection
N C Vega, R Wallar, J Caram et al.
- Optical properties of excitons in ZnO-based quantum well heterostructures
T Makino, Y Segawa, M Kawasaki et al.

Recent citations

- Suppression of the green emission, texturing, solute-atom diffusion and increased electron-phonon coupling induced by Ni in sol-gel ZnNiO thin films
Oscar Marin *et al*
- First-Principles Investigation of Size-Dependent Piezoelectric Properties of Bare ZnO and ZnO/MgO Core-Shell Nanowires
Ye Wu *et al*
- ZnO nanowire sensitization with Ru polypyridyl complexes: charge-transfer probed by spectral and relaxation photocurrent measurements
N C Vega *et al*

IOP ebooks™

Bringing you innovative digital publishing with leading voices to create your essential collection of books in STEM research.

Start exploring the collection - download the first chapter of every title for free.

This content was downloaded from IP address 190.3.119.146 on 20/12/2018 at 19:11

IOP Publishing Nanotechnology
Nanotechnology **28** (2017) 275702 (9pp) https://doi.org/10.1088/1361-6528/aa7454

The shell effect on the room temperature photoluminescence from ZnO/MgO core/shell nanowires: exciton–phonon coupling and strain

N C Vega[1], O Marin[1,2], E Tosi[1], G Grinblat[1], E Mosquera[2,3], M S Moreno[4], M Tirado[5] and D Comedi[1,6]

[1] NanoProject and Laboratorio de Física del Sólido, Depto. de Física, FACET, Universidad Nacional de Tucumán, Av. Independencia 1800, 4000 Tucumán, Argentina—CONICET, Argentina
[2] Laboratorio de Materiales Funcionales a Nanoescala, Departamento de Ciencias de los Materiales, Facultad de Ciencias Físicas y Matemáticas, Universidad de Chile, Beauchef 851, Santiago, Chile
[3] Departamento de Física, Universidad del Valle, A A 25360, Cali, Colombia
[4] Centro Atómico Bariloche, 8400—San Carlos de Bariloche, Argentina
[5] NanoProject and Laboratorio de Nanomateriales y Propiedades Dieléctricas, Depto. de Física, FACET, Universidad Nacional de Tucumán, Av. Independencia 1800, 4000 Tucumán, Argentina—CONICET, Argentina

E-mail: dcomedi@herrera.unt.edu.ar

Received 17 February 2017, revised 5 May 2017
Accepted for publication 19 May 2017
Published 9 June 2017

Abstract

The room temperature photoluminescence from ZnO/MgO core/shell nanowires (NWs) grown by a simple two-step vapor transport method was studied for various MgO shell widths (w). Two distinct effects induced by the MgO shell were clearly identified. The first one, related to the ZnO/MgO interface formation, is evidenced by strong enhancements of the zero-phonon and first phonon replica of the excitonic emission, which are accompanied by a total suppression of its second phonon replica. This effect can be explained by the reduction of the band bending within the ZnO NW core that follows the removal of atmospheric adsorbates and associated surface traps during the MgO growth process on one hand, and a reduced exciton–phonon coupling as a result of the mechanical stabilization of the outermost ZnO NW monolayers by the MgO shell on the other hand. The second effect is the gradual increase of the excitonic emission and decrease in the defect related emission by up to two and one orders of magnitude, respectively, when w is increased in the ~3–17 nm range. Uniaxial strain build-up within the ZnO NW core with increasing w, as detected by x-ray diffraction measurements, and photocarrier tunneling escape from the ZnO core through the MgO shell enabled by defect-states are proposed as possible mechanisms involved in this effect. These findings are expected to be of key significance for the efficient design and fabrication of ZnO/MgO NW heterostructures and devices.

Keywords: ZnO nanowires, ZnO/MgO core/shell, ZnO pholuminescence, ZnO exciton–phonon coupling, strain

(Some figures may appear in colour only in the online journal)

[6] Author to whom any correspondence should be addressed.

 © 2017 IOP Publishing Ltd Printed in the UK

1. Introduction

In nanoscale semiconductors, surface effects play a dominant role in determining their photonic and optoelectronic characteristics. Therefore, a considerable amount of research has been dedicated to understanding and engineering these effects. In particular, the ZnO nanowire (NW) is a very interesting nanomaterial due to its high exciton binding energy (60 meV), direct wide bandgap (3.4 eV), piezoelectricity, among many other useful properties. Based on this nanomaterial, numerous applications have been demonstrated in the past years, such as UV LEDs [1], photodetectors [2], solar cells [3], UV lasers [4], and ultrasensitive gas and biological sensors [5]. To achieve optimal emission in the UV, the 'passivation' of surface states that inhibit excitonic recombination through competing non-radiative or radiative transitions involving deep states producing spurious visible luminescence has proven to be of key importance [6, 7]. The strategy of covering the ZnO NW with a MgO shell has been shown to be a promising approach to address this issue [8–11]. MgO has a very wide bandgap (7.8 eV), and provides high potential barriers that can efficiently confine excited carriers within the ZnO core conduction and valence bands. Nevertheless, the physical passivation mechanism that leads to the observed improvements of the UV photonic properties has remained elusive. Some authors have suggested that the MgO shell physically removes oxygen vacancies or other defects from the ZnO NW walls, thus eliminating recombination channels that compete with the excitonic recombination [12–14]. Others have suggested that the improved UV emission results from a dielectric screening effect provided by any dielectric shell [15]. Very recently, it has been suggested that passivation in nanosystems is not based on the elimination of surface states, but on the mechanical stabilization of the nanosurfaces [16].

In this work, we study this problem in ZnO/MgO core/shell NWs with various shell widths (w). Besides examining their morphology and structure, we analyze the dependence of their photoluminescence (PL) spectrum on w. We find that a thin MgO shell of a few monolayers is not enough to fully passivate the detrimental surface effects on the PL. Instead, we observe a gradual increase (decrease) in the PL intensity for the UV (visible) band as w is increased. Only when w reaches sufficiently large values ($w > \sim 17$ nm) optimal passivation is attained. Furthermore, we find evidence for significant reduction of the exciton–phonon coupling in the PL spectra and for strain build-up on the ZnO core in x-ray diffractograms, both induced by the MgO shell. The overall analysis of the experimental data suggests that the UV emission enhancement in the core/shell NWs involves complex mechanisms that may include elimination of adsorbates, mechanical stabilization of the ZnO NW interface, and strain.

2. Experimental details

The ZnO/MgO core/shell NWs were fabricated via a two-step vapor transport and deposition method under controlled ultra-high purity Ar and O_2 flows on Au-nanocluster covered silicon substrates, as described in [10]. In a first stage, various ZnO NW samples were grown under identical conditions, using ZnO + graphite powder (1:1 in weight) at 1100 °C as the vapor source and substrates placed at 21 cm from the vapor source downstream the quartz tube (substrate temperature ~870 °C). Then, in a second stage, Mg powder at $T_{Mg} = 700$ °C was employed as vapor source, and different growth times and substrate-source distances were used to produce ZnO/MgO core–shell NW samples with various MgO-shell thicknesses. The substrate temperatures (~600 °C–650 °C) were always low enough to suppress interdiffusion between core and shell while producing significant Mg vapor supersaturation for the shell growth [10]. For both fabrication steps, the Ar and O_2 flow rates were controlled at 125 sccm and 8 sccm, respectively.

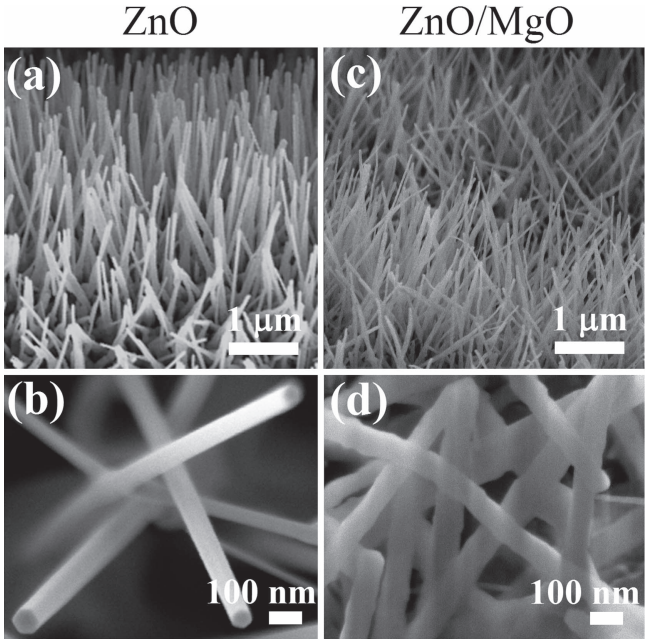

Figure 1. SEM images with different magnifications of a ZnO NW sample (a), (b) and of a ZnO/MgO core/shell NW sample (c), (d). As observed in (b), the ZnO NWs are highly crystalline exhibiting hexagonal cross-section expected from wurtzite c-axis alignment.

High resolution transmission electron microscopy (HRTEM) images were acquired using a Tecnai F20 G^2 UT transmission electron microscope operated at room temperature and 200 kV. Scanning electron microscopy (SEM) images were obtained with a *Zeiss Supra* 55 *VP* and a *Zeiss Supra* 40 field emission microscope. X-ray diffraction measurements were performed in some of the samples using a Bruker D8 Advance diffractometer equipped with Cu Kα radiation source ($\lambda = 1.5418$ Å). The power generator was set to 40 kV and 30 mA and the patterns were recorded in the 30°–80° range.

PL measurements were carried out at room temperature and ambient conditions on the as grown NWs on their Si substrate with a 15 mW He–Cd laser from Kimmon Koha Co. using the 325 nm line as the excitation source (2 mm diameter

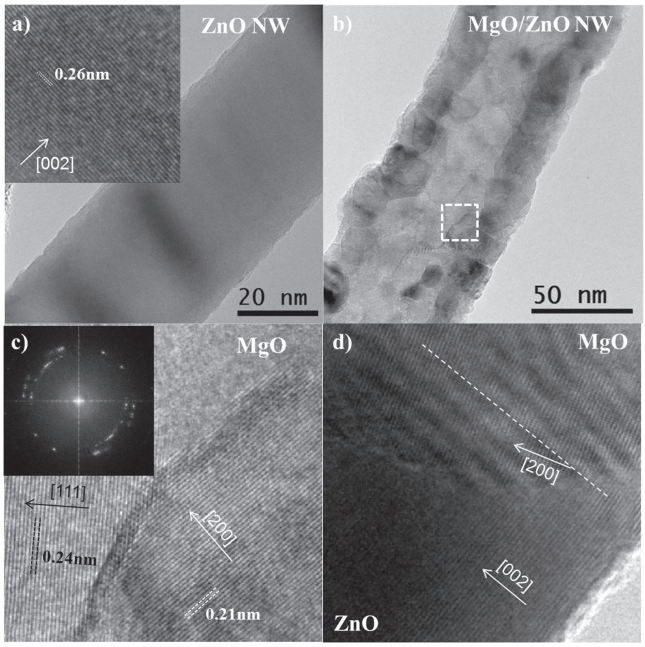

Figure 2. HRTEM images of a ZnO NW (a) and of a ZnO/MgO core/shell NW (b). The image in (c) shows a high magnification image of the MgO shell shown in the rectangle in (b), indicating the different MgO lattice planes that are observed. (d) A region of another NW where the ZnO core remained partially uncovered by the MgO shell, a part of which can be also seen.

beam spot). The emission was collected in a back-scattering geometry with an AvaSpec-ULS3648 spectrometer.

3. Results

3.1. Morphology and structure

Figures 1(a), (b) show SEM images for different magnifications of ZnO NWs prior to their covering with MgO. The mean NW length is about 1 μm, with a corresponding mean diameter of 60 nm. As it is observed in figure 1(b), the NW cross-sections are hexagonal, corresponding to growth along the *c*-axis of the wurtzite crystal structure. Figures 1(c), (d) exhibit SEM images of ZnO NWs covered with a thin ($\sim$10 nm) MgO shell. Due to the lattice mismatch between ZnO and MgO, and differences in the thermal expansion coefficient, the core/shell structure is strained so NWs are slightly bent [10]. The non-planar, slightly rough morphology of the MgO shell (see figure 1(d)) indicates a polycrystalline structure, as has been observed before in MgO shell growth from the vapor phase on *c*-axis oriented ZnO NWs [9].

HRTEM images of a bare ZnO and a ZnO/MgO core–shell NWs are shown in figure 2. In agreement with the hexagonal cross section observed in the SEM image in figure 1(b), the bare ZnO NW (figure 2(a)) is found to be single crystalline, with its axis aligned along the *c*-axis of the wurtzite structure, with interplanar distance of 0.26 nm corresponding to the expected value for relaxed wurtzite ZnO (002). The HRTEM image for a MgO covered ZnO NW shown in figure 2(b) clearly shows a highly textured polycrystalline nature of the MgO shell. Crystallite sizes range between 5 and 20 nm. Figure 2(c) is a zoom view of a typical region between crystallites, where crystallographic planes can be readily recognized. Two different orientations, namely the [111] and [200] directions in the rock-salt structure of MgO, with their corresponding interplanar distances of 0.24 and 0.21 nm, are seen. As a matter of fact, analysis of whole NW shells reveals the presence of only these two crystallographic directions, indicating the MgO is highly textured. This is shown by the diffraction pattern in the pole figure depicted in the inset of figure 2(c), where spots along the rings corresponding to the {111} and {200} crystallographic planes are observed. Figure 2(d) shows a region in another NW within the ensemble where a part of the ZnO NW core was left uncovered by the MgO shell. The relative orientation between the ZnO (002) and the MgO (200) planes in this case is 17°. However, we find that this is not a rule but only part of a broad in-plane distribution of MgO crystallite orientations as determined by direct inspection into numerous crystallites along the shells.

Table 1. MgO mean shell width (w) for different ZnO/MgO NW samples fabricated, and the corresponding Mg source-sample distance (D) employed for each MgO deposition. Estimated uncertainties are expressed between parentheses.

D (cm)	12	13	14	15	16	17
w (nm)	20 (3)	18 (3)	14 (2)	10 (2)	7 (2)	3 (2)

By measuring diameters of core–shell NWs on several SEM images, it was possible to determine approximate MgO mean shell widths (w). Table 1 exhibits these w values for NW samples grown at different substrate-Mg source distances (D) during the MgO shell growth. The value of w diminishes for larger distances D, as expected and understood from a reduction in the Mg metal vapor partial pressure and supersaturation over the ZnO NWs with increasing metal source-substrate distance [7, 10].

The crystalline phases present in the samples were also studied using XRD. Figure 3 shows typical diffractograms for bare ZnO NWs and two different ZnO/MgO core/shell NW samples. As can be seen, the high intensity of the ZnO (002) peak indicates preferential orientation along the wurtzite *c*-axis, in agreement with the SEM and HRTEM results. However, weak diffraction peaks corresponding to other ZnO planes are also seen [(101), (102), (103) and (110)], which stem from the finite width of the NW orientation distribution about the substrate normal. For the ZnO/MgO core/shell NWs, the MgO (200) diffraction peak from the thin MgO shells is detected. Also, peaks due to a Mg_2Si phase appear at $\sim$40° (220) and $\sim$58° (400), which result from the reaction of Mg vapor with the Si substrate during the MgO coating process.

Figure 4 shows a close up of the diffraction pattern in the region of the ZnO (002) reflection for NW samples with different shell widths. The skewed peak shapes towards higher angles are due to the doublet character of the Cu x-ray source ($K_{\alpha 1}$ and $K_{\alpha 2}$). However, it is clear that the deposition

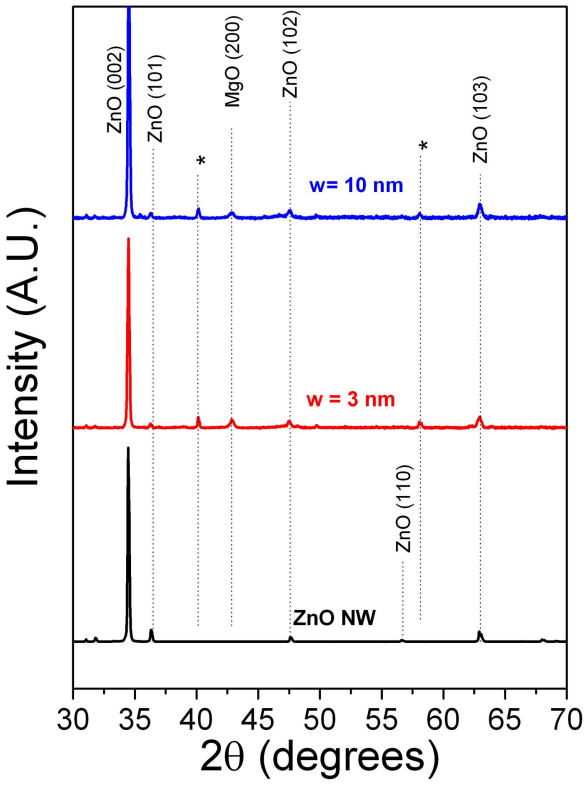

Figure 3. XRD patterns from a ZnO NW sample (bottom) and for two ZnO/MgO core/shell NW samples with different MgO mean shell widths w. The different phases on the samples are identified and indicated. The peaks identified by (*) correspond to the (400) and (220) peaks of a Mg_2Si phase created during the MgO shell deposition due to reaction of Mg atoms with the Si substrates upon which the ZnO NWs were grown.

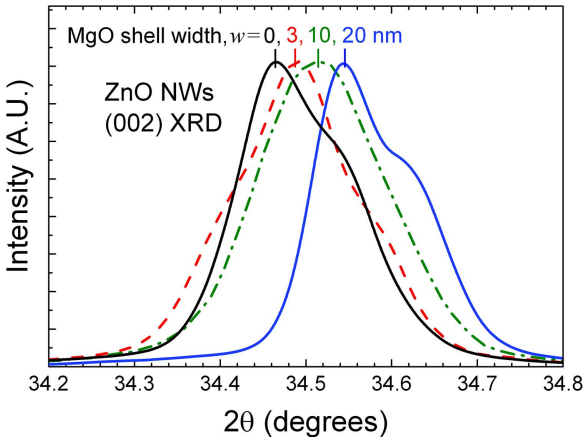

Figure 4. Bragg x-ray reflections corresponding to the (002) planes from ZnO wurtzite observed in the XRD patterns from ZnO NWs and from core/shell ZnO/MgO NWs with different MgO mean shell widths w.

of the MgO shell produces an overall upward shift of the ZnO (002) peak. This effect can be interpreted as a reduction of the interplanar spacing along the c direction within the NWs, and can be expected from a uniaxial compressive stress resulting from the smaller MgO interplanar spacings.

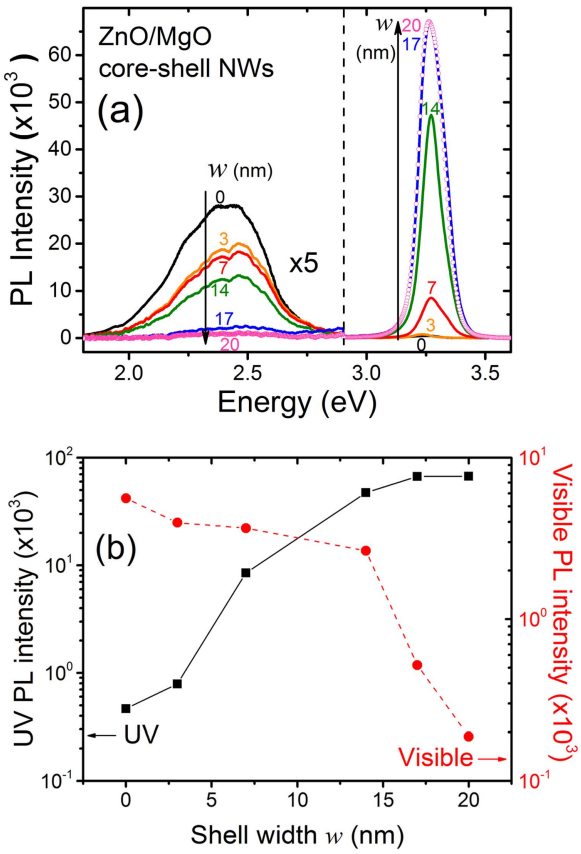

Figure 5. (a) PL spectra from the ZnO NW and the ZnO/MgO core/shell NW samples. The arrows in the figures indicate increasing w. (b) Dependence on w of the UV (black squares) and visible (red dots) PL peak intensities. Note the logarithmic scales. The lines are guides to the eyes.

3.2. Photoluminescence

The PL spectra from the ZnO/MgO core–shell samples are presented in figure 5(a). They exhibit the typical excitonic PL band in the UV (centered at ∼380 nm (3.26 eV)) and a deep defect-related PL band in the visible (centered near 510 nm (2.43 eV)) [10, 11]. As can be seen in figure 5(a), the excitonic PL intensity increases gradually as w is increased, while the opposite occurs for the visible band. This behavior is also evident from figure 5(b), which exhibits the PL peak intensity for both bands as a function of w. Note that the excitonic PL in the UV increases by more than two orders of magnitude and seems to saturate for $w > \sim 17$ nm. We have checked and found no further improvement in the UV optical performance for up to several hundred nanometers shell widths. In contrast, the defect related PL decreases by a factor of 2–3 for w between 0 and 14 nm, and then decreases strongly for w between 14 and 20 nm. These findings clearly reveal two interesting facts. First, a considerably thick MgO shell of at least ∼70–80 MgO monolayers is needed to achieve optimal passivation of the ZnO NW surface (i.e., saturation of the UV PL for $w > \sim 17$ nm). Therefore, the PL improvement cannot be ascribed to just the physical removal of defects (such as the filling of O vacancies, for instance) originally present at the ZnO NW walls, or the desorption of ambient adsorbates (such

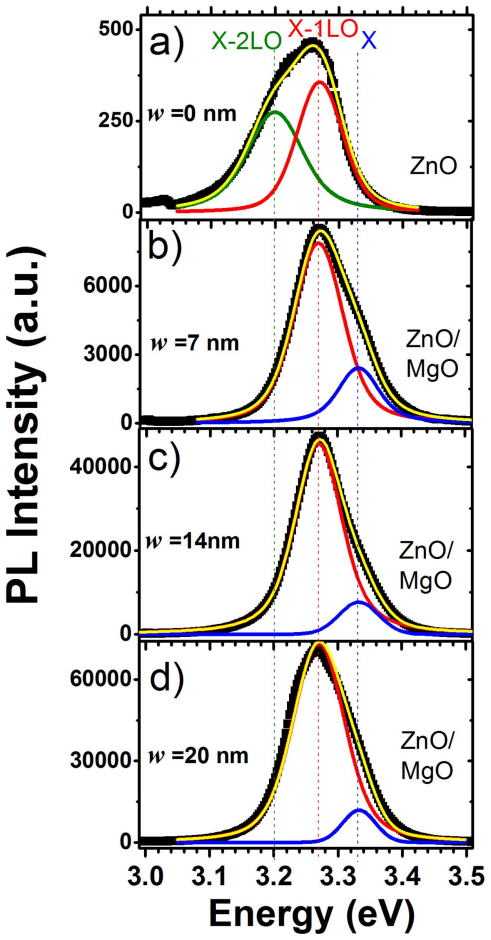

Figure 6. Experimental (black symbols) and fitted (yellow lines) PL spectra from ZnO (a) and from ZnO/MgO core/shell NW samples (b)–(d) for different MgO shell widths, w, in the UV region. The components of the fits attributed to the excitonic emission (X) and its phonon replica (X-1LO, X-2LO) are indicated by vertical dashed lines (positions) and by blue, red, green colors, respectively. Note the very different vertical scales in (a)–(d).

as O_2), as these processes should be completed after depositing a few MgO monolayers. Note that recently [12], a MgO shell width of 15 nm was reported for optimal surface passivation of ZnO NWs grown by photoassisted metal-organic chemical vapor deposition, which is in close agreement with the w value suggested by figure 5. The second interesting finding from the data in figure 5(b) is the different w values for which the UV and the defect-related PL intensities show their larger changes. This shows that the changes in the PL intensities with w are not (only) due to a competition between the excitonic and defect-related radiative processes giving rise to these bands, but reflect particular features of each recombination process and their changes with w.

In order to explore more deeply the nature of the PL intensity increase with increasing w, we analyze the PL peak due to excitonic emission in the UV. This is shown in figure 6, where we have deconvoluted the peak using the well-known fact that at room temperature, the UV PL peak in ZnO is in general dominated by the phonon replicas of the free exciton emission [17]. Indeed, in figure 6(a) we observe that the UV emission from bare ZnO NWs can be described by peak components centered at $E_1 = 3.27$ eV and $E_2 = 3.20$ eV, i.e., the energy difference between these peaks is very close to the LO phonon energy of ZnO ($\hbar\omega_{LO} \approx 71$ meV). Hence, the E_1 and E_2 peaks can be tentatively ascribed to the first (X-1LO) and second (X-2LO) exciton phonon replicas peaked at $E_X - \hbar\omega_{LO} + \Delta E$ and $E_X - 2\hbar\omega_{LO} + \Delta E$, where E_X, is the energy of the excitonic (X) emission, $\hbar\omega_{LO}$ is the LO phonon energy in ZnO and ΔE is the kinetic energy of the free excitons [17]. However, with the MgO shell deposition, together with the strong intensity increase, a significant change of the peak shape is observed (see figures 6(b)–(d)). In contrast to the case in figure 6(a), the UV peaks are now skewed towards the high energy side, with corresponding fitting components at 3.33 and 3.27 eV. The peak at 3.33 eV is very close to the expected value for E_X at room temperature, while the second peak is just at the same position as peak E_1. The energy difference between these two peaks obtained from the fits in figures 6(b)–(d) is 63 meV, i.e. very close to the value found by others and attributed to the value of $\hbar\omega_{LO}$ - ΔE expected for the difference between the X and X-1LO emissions [17]. Hence, we attribute the peak at 3.33 eV as the X emission, in consistency with our previous attribution of the components at $E_1 = 3.27$ eV and $E_2 = 3.20$ eV as its first and second phonon replica (X-1LO and X-2LO). Note that the overall PL peak shape and the relative contributions of the two dominant components for the ZnO/MgO core/shell NWs in figures 6(b)–(d) exhibit little change with increasing w.

4. Discussion

From the PL measurements (figures 5 and 6), we see that the deposition of the MgO shell produces not just a strong decrease of the defect emission and increase of the excitonic PL intensity (figure 5), but also a change in the excitonic PL peak shape, which is due to the suppression of the X-2LO replica and a strengthening of the X component (compare figures 6(a) and (b)). It is interesting to note that the PL peak shape does not further change significantly with increasing w (figures 6(b)–(d)); in contrast the total excitonic PL peak intensity increases by orders of magnitude when w increases from 3 to 17 nm (figure 5). Hence, we make a distinction between two effects induced by the MgO shell: one is the asymmetry change that occurs for any w (see figures 6(b)–(d)) as compared to the bare ZnO NW case (figure 6(a)), and hence it is essentially independent of w and therefore is *interface-related*, and another effect that depends on w, which is the further strong increase in the excitonic emission and the reduction of the defect emission (figure 5). In an effort to shed light into the possible mechanisms that apply in these two effects, we next discuss in detail the process of MgO shell fabrication and its possible impacts on the ZnO NW electronic structure and PL.

4.1. From a ZnO/air to the ZnO/MgO interface

As known from electrical conductivity and photoconductivity measurements [11], as well as from electron spin resonance [18] and photoelectron spectroscopy studies [19], electrons are strongly trapped at the ZnO NW walls/air interfaces, resulting in strong band bending and surface depletion layers of several nanometers wide that can render a thin NW fully depleted. The trapping of free electrons is believed to be mainly provided by physisorbed atmospheric O_2 and H_2O molecules via surface states [20]. Because of the strong conduction and valence band bendings taking over the whole ZnO NW cross section, photoexcited electrons and holes generated during a PL experiment will be in general drifted in opposite directions along the NW radial lines, electrons accumulating at the NW center and holes at the NW surface. This spatial separation of electrons and holes tends to inhibit the excitonic recombination and UV emission, thus favouring competing recombination channels, such as surface-state related transitions leading to both, increased PL in the visible (via deep surface defect states) and non-radiative recombination (via multi-phonon processes) [7, 15]. Indeed, it is well known that the green emission band intensity in ZnO nanostructures correlates with the specific surface area and hence is related to defects at the nanostructure surfaces [7].

However, prior to MgO growth by vapor transport, the bare ZnO NWs are heated to above 600 °C in $Ar + O_2$ atmosphere, and hence most physisorbed species are desorbed. This, by itself, already reduces the electron trap density at the ZnO NW walls and the surface band bending [19]. Since the ZnO NW core becomes further encapsulated and shielded from further exposure to atmospheric adsorbates by the MgO shell, this situation should be preserved when the NWs are taken out to the atmosphere for PL measurements. Furthermore, the newly formed ZnO/MgO interface could involve the creation of new intrinsic interface traps due to lattice and thermal mismatches. The net result, however, is a reduced trap density at the ZnO NW core surface, and reduced band bending and depletion layers in the MgO/ZnO core/shell NW as compared to the bare ZnO NW, as evidenced by the excitonic PL intensity increase and the defect PL in the visible decrease (figure 5(b)). Note that this interpretation (reduced band bending leading to PL improvement) is in line with our previous electrical measurements on single NWs, where the resistance was seen to fall by various orders of magnitude for ZnO/MgO core/shell NWs as compared to that measured on bare ZnO NWs [11].

As for the excitonic PL peak shape change from figures 6(a)–(d), it results from a complete suppression of the X-2LO phonon replica, which is accompanied by a strong enhancement of the X and X-1LO relative contributions. This is clearly due to a change in the exciton–phonon coupling, which may arise from a change in the phonon wavefunction near the interface with respect to the exciton wavefunction in real space when the MgO shell replaces the air at the ZnO NW walls, as reported for core–shell nanoparticles [21]. The Zn and O atoms at the nearly free surface of the ZnO NW nonpolar surfaces are loosely constrained, have large vibration amplitudes (i.e. 'soft surfaces' [16]) and hence large exciton–phonon interaction there. As the MgO shell is deposited, the Zn and O atoms become more constrained and mechanically stabilized and the exciton–phonon interaction is reduced. The exciton–phonon interaction in ZnO is dominated by the long-range Fröhlich interaction of the electron and hole comprising the exciton with the polarization field generated by the atomic vibrations in the strongly polar ZnO lattice [22]. First order processes, such as the X-1LO recombination, are not allowed in perfect crystals due to parity conservation. However, this rule may be relaxed in the presence of crystal imperfections which introduce additional intermediate states of alternating parity into the Fröhlich scattering mechanism. This generally occurs at the semiconductor surfaces and hence Raman and PL studies on ZnO NWs have revealed exciton–phonon coupling changes as evidenced by changes in the X-2LO/X-1LO emission intensity ratio upon surface morphology changes in ZnO NWs with sizes from about 30 nm to several hundred nanometer diameters [22, 23]. Similarly, the X-2LO/X-1LO ZnO ratio has been found to be also sensitive to (an increasing function of) the NW size up to at least 100 nm diameter [24], which results from an increasing exciton–phonon coupling with increasing sample size as expected from the Fröhlich-type interaction.

The reduced band bending due to the reduction of the trap density at the ZnO NW surface upon the MgO shell deposition can explain the PL UV emission enhancement (by ~70%) and diminishing defect emission (by ~30%) observed in figure 5(b) for the thinnest MgO shell. However, what happens when w is increased? We do not expect further reduction in the interface trap density because it should be fixed by the MgO shell deposition conditions, which are virtually the same for all w. Hence, in an effort to understand the further PL improvements with increasing w, we need to consider additional mechanisms.

4.2. Increasing the MgO shell width

When the shell width is increased between few nanometers up to about 17 nm, the excitonic PL intensity in the UV increases by more than 2 orders of magnitudes and the defect-related emission intensity in the visible decreases by almost two orders of magnitude (figure 5), such that the UV/visible ratio increases by up to 4 orders of magnitude, while the excitonic PL peak shape does not change significantly (figures 6(b)–(d)). This means that the accumulating material on the MgO shell is further improving the excitonic radiative recombination, however without further altering the phonon–exciton coupling responsible for the phonon replica of the excitonic emission. We note that previous reports have not discussed the distinct effects that occur neither upon ZnO/MgO interface formation nor upon increase of the MgO shell width. For instance, it has been frequently assumed that the beneficial role of the MgO shell on the PL spectra is related to electron transfer across the ZnO/MgO interface [25], which would fill the depletion layer within the NW core. However, MgO layers are typically insulating and their carrier densities are

very low. Differently to what happens with most transition metal oxides including ZnO, MgO is not intrincally n-type doped by native defects (which tend to form deep rather than shallow donor levels) nor doped by H or other impurities (which also form deep electronic levels) [26]. Noting this, some authors proposed that photocarriers could be generated within the shell during the PL measurement and then fall into the core [12]. However, this effect is negligible for our PL experiments (as experimentally verified [10]), since our PL excitation energy is smaller than half the MgO bandgap energy. Hence, the effects observed here would not be explained by electronic transfer from the shell to the core.

Another model that has been invoked involves a so-called 'dielectric screening' of the trapped charges at the ZnO NW surface [15], inspired by the fact that enhancements of the UV emission in ZnO NWs occur as well when covered with shells of other dielectric materials, such as polymers. According to this model, the trapped charges at the ZnO/MgO interface would induce a polarization field in the shell which, in turn, would screen the inner electric field within the ZnO core reducing the band bending. However, no polarization within the dielectric shell is actually expected to occur due to the trapped charges at the ZnO/MgO interface, since these charges essentially come from the ZnO core, and are the ones that leave there a depletion layer in the first place. Indeed, since the immobile ionic charge left behind in the ZnO compensates for this trapped charge, the net charge within the NW core turns out to be zero, with no polarizing field induced on the outer MgO shell (following Gauss law). Even if some of the mobile charge would spill out of the ZnO core during MgO shell growth and become trapped at the MgO shell outer surface, electrostatic calculations (not shown) reveal that the resulting polarization within the MgO shell would not lead to any w-dependent effect on the core. Hence, with these considerations, the dielectric screening effect cannot explain the PL improvements that occur with increasing w.

In is interesting to note that the compressive strain buildup on the ZnO core, as deduced from the XRD data in figure 4, is also an increasing function of MgO shell width, w. The lattice mismatch for the MgO/ZnO heterostructure can be significant (up to ~6%, as deduced from the ZnO and MgO lattice parameters). In practice, much of the mismatch elastic energy in the ZnO/MgO core/shell NW is relaxed by NW warping, as reported previously [10, 11], and also by stacking fault and grain boundary formation within the MgO shell [9]. Figure 7 shows the calculated c parameter from the ZnO (002) Bragg reflection from the XRD data in figure 4(b), for the different studied samples, as a function of w. The corresponding strain, which is negative and therefore evidences a uniaxial compressive stress exerted by the shell on the core, is on the order of tenths of a percent and increases in absolute value with increasing w. The stress is compressive because of the smaller MgO lattice parameter and interatomic distances as compared to those for ZnO. The strain on the ZnO core increases with w because while for $w \ll r$ (where r is the NW radius) most of the strain occurs within the shell, as w becomes comparable to r, more interface strain is increasingly transferred from the MgO shell to the ZnO core [27].

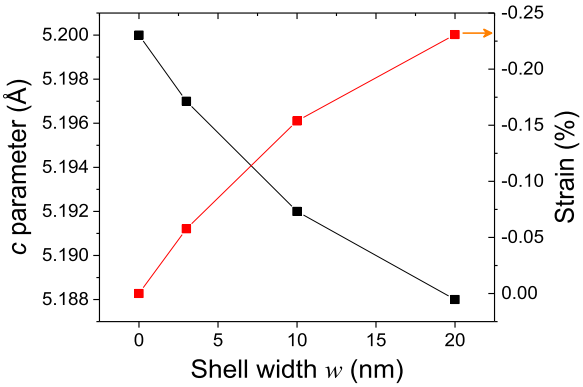

Figure 7. ZnO c parameter and corresponding strain buildup, as determined by XRD from core–shell ZnO-MgO NW samples, as a function of the mean MgO shell width, w. The lines are guides to the eye.

While the observed strain has been reported to produce shifts of only a few meV in the bandgap energy [28], consistent with the lack of noticeable shifts in the excitonic PL component and its phonon replica when changing w (figure 6), it can be large enough to produce strong effects at the MgO/ZnO interface [29]. Such inhomogeneous strain, which partially relaxes far from interfaces, has been very recently measured using a focused x-ray beam diffraction technique for another core/shell hexagonal wurtzite NW system (GaN/InGaN) [30]. The uniaxial compressive strain is found to be accompanied by in-plane strains as well, in consistency with the Poisson effect. Moreover, since the uniaxial strain occurs along a polar direction of the wurtzite structure, it induces a polarization potential (the piezoelectric potential) that is maximum at the heterostructure interface and increases with w, thus providing a mechanism for w-dependent changes in the band-bending profile across the NW core cross section [31]. As for the ZnO/MgO system, measurements of local strain profile near the MgO/ZnO interface would be essential to determine whether the associated changes of the band-bending profile would suffice to explain the strong PL enhacements observed. Futhermore, a model would be needed to relate this strain profile and its effects on the electronic properties through the piezoelectric potential across the NW cross section and axis. Clearly, more experimental and modeling work on this issue is needed.

However, before closing this discussion, we would like to briefly point to an additional mechanism that could also be involved in the strong w dependence of the excitonic PL intensity, which is photocarrier defect-mediated tunneling across the MgO shell to surface states. The MgO/ZnO is a type I interface with large barriers for both photoelectrons and photoholes (at least 1.7 and 1.2 eV, respectively [32]) due to the large MgO bandgap energy, so tunneling escape probabilities for both carriers should be negligible for shell widths as small as ~1 nm for a perfectly crystalline MgO shell. However, the tunneling probabilities are expected to become significant (in the nanometer scale) if the tunneling barrier height is determined by a MgO midgap state band. Such energy bands can occur in our MgO shell due to a relatively

large density of defects at grain boundary regions as those observed in the HRTEM images of figure 2. Indeed, large carrier tunneling currents have been deduced across a MgO shell with $w \approx 10$ nm from the enhanced performance of ZnO/MgO core–shell NW-based solar cells [33]. This w value is comparable to those explored here. Moreover, the much lower than expected barrier heights due to defect-mediated tunneling is a well-known fact from the extensive uses of MgO as a tunneling barrier in spintronic devices [34]. Hence, we suggest that a photocarrier escape channel from the ZnO core through the MgO barrier to MgO surface states could provide an additional non-radiative recombination mechanism competing with excitonic radiative recombination. Given that the tunneling probability for such a mechanism should decrease with increasing w, the lifetime of this additional non-radiative recombination channel should increase until becoming negligible, leading to an excitonic PL intensity increase until saturation as observed in the experimental data of figure 5.

4.3. The interplay between the excitonic and defect-related emissions

A point that needs further discussion is the interesting different behavior between the excitonic and defect-related PL intensity changes with increasing w revealed in figure 5(b). The excitonic PL intensity exhibits orders of magnitude increase for $0 < w < 14$ nm while the defect-related PL shows only a slow decrease in this region, whereas the latter diminishes pronouncedly for $14\text{ nm} < w < 20$ nm in coincidence with the excitonic PL intensity reaching a saturation. We believe this is associated with the nature of the recombination mechanism leading to the defect-related emission in ZnO NWs. After many years of debate, there is some consensus considering this well-known 'green emission' as a result of conduction band electrons recombination with holes trapped at deep oxygen vacancy defects at the NW walls [7, 35]. Note that the accumulation and trapping of holes at the NW surface is favored by the band bending profile along the NW radius. Recently, ultrafast spectroscopy studies in ZnO NWs fabricated by a similar growth method as the one used here were able to determine an ultrafast excitonic Auger-type hole trapping mechanism, which explains the high efficiency of this recombination channel and the strong green PL from ZnO NWs without a MgO shell [35]. A feature of the excitonic Auger-type hole trapping process is its strong increase with increasing exciton density. We consider this recombination mechanism to explain the particular behavior of the defect-related PL intensity with increasing w observed in figure 5(b). Consider the initial reduction of the band bending for small w which, as discussed in section 4.1, leads to a reduction of the number of holes reaching the ZnO NW walls. This tends to reduce the number of trapped holes (and hence we observe a reduction of the defect-related emission in the visible) but, because of the surviving holes in the valence band, it also leads to an increase of the effective exciton density (which ultimately results in the observed increased excitonic UV PL intensity with increasing w in figure 5(b)). However, this increased exciton density will also cause an increased Auger-type trapping probability, thus partially compensating the band bending reduction impact on the defect-related emission and giving a rationale to explain the slow variation of this intensity for $0 < w < 14$ nm.

Conversely, when the exciton density reaches a saturation (as experimentally evidenced by the saturation of the UV PL intensity for large w in figure 5(b)), so will its influence on the excitonic Auger-type hole trapping, and therefore its compensating impact on the band bending reduction effect will stop increasing with w, leading to a stronger reduction of the defect-related PL intensity for $14\text{ nm} < w < 20$ nm.

Of course, a full understanding of the recombination physics would need further studies which would include PL time decay and temperature dependence on core/shell ZnO/MgO NWs with different shell widths, to determine changes in exciton dynamics, charge trapping at luminescent centers and non-radiative recombination lifetimes with increasing w.

5. Conclusions

We have used SEM, HRTEM, XRD and PL measurements to study the morphology, structure and optical properties on ZnO/MgO core/shell NWs with fixed mean ZnO core radius and varying mean MgO shell width (w) grown by a simple two-step vapor transport method.

We have identified two distinct effects in the PL spectra. The first one is related to the change from the ZnO/air to the ZnO/MgO interface, which produces an overall increase by 70% of the excitonic PL intensity and a 30% decrease of the defect related PL, a complete suppression of the X-2LO phonon replica and a strong enhancement of the X PL emission. Reduction of the band bending following the removal of atmospheric adsorbates and their associated surface states, and reduced exciton–phonon coupling upon the formation of the new ZnO/MgO interface as a result of the mechanical stabilization of the outermost ZnO NW monolayers by the MgO shell, are proposed to explain this effect.

The second effect involves the gradual increase of the excitonic PL and decrease of the defect related emission with increasing w by up to two and one orders of magnitude, respectively. Uniaxial strain build-up within the ZnO NW cores with increasing w, as detected by XRD measurements, and photocarrier escape from the ZnO core through the MgO shell by midgap state mediated tunneling are proposed as possible mechanisms involved in this effect.

These findings should be of key significance for the efficient design and fabrication of ZnO/MgO NW heterostructures and devices, and are expected to promote further studies on the physics of charge recombination in core/shell ZnO/MgO NWs and its changes with varying MgO shell thickness.

Acknowledgments

We are grateful to Dr Joseba Orive from the LMFN, Departamento de Ciencias de los Materiales, FCFM, Universidad de

Chile for help with the XRD measurements. In Argentina, this work was partially funded by the National University of Tucumán (PIUNT 26/E535 and 26/E439) and FONCyT-ANPCyT (PICT2010-400 and PICT2015-0865); in Chile by FONDECYT (Postdoctorado No. 3160043 and Regular No. 1150475).

References

[1] Chen M T, Lu M P, Wu Y J, Song J, Lee C Y, Lu M Y, Chang Y C, Chou L J, Wang Z L and Chen L J 2010 Near UV LEDs made with *in situ* doped p–n homojunction ZnO nanowire arrays *Nano Lett.* **10** 4387–93

[2] Soci C, Zhang A, Xiang B, Dayeh S A, Aplin D P R, Park J, Bao X Y, Lo Y H and Wang D 2007 ZnO nanowire UV photodetectors with high internal gain *Nano Lett.* **7** 1003–9

[3] Son D, Im J, Kim H and Park N 2014 11% efficient perovskite solar cell based on ZnO nanorods: an effective charge collection system *J. Phys. Chem.* C **118** 16567–73

[4] Vanmaekelbergh D and van Vugt L K 2011 ZnO nanowire lasers *Nanoscale* **3** 2783–800

[5] Wang L, Kang Y, Liu X, Zhang S, Huang W and Wang S 2012 ZnO nanorod gas sensor for ethanol detection *Sensors Actuators* B **162** 237–43

[6] Voss T, Bekeny C, Gutowski J, Tena-Zaera R, Elias J, Ĺvy-CÍment C, Mora-Seró I and Bisquert J 2009 Localized versus delocalized states: photoluminescence from electrochemically synthesized ZnO nanowires *J. Appl. Phys.* **106** 10–4

[7] Grinblat G, Capeluto M G, Tirado M, Bragas A V and Comedi D 2012 Hierarchical ZnO nanostructures: growth mechanisms and surface correlated photoluminescence *Appl. Phys. Lett.* **100** 233116

[8] Yang H Y, Yu S F, Li G P and Wu T 2010 Random lasing action of randomly assembled ZnO nanowires with MgO coating *Opt. Express* **18** 13647–54

[9] Wu Y, Wu W, Zou X M, Xu L and Li J C 2012 Growth and great UV emission improvement of highly crystalline quality core–shell ZnO/MgO nanowires *Mater. Lett.* **84** 147–50

[10] Grinblat G, Borrero-González L J, Nunes L A O, Tirado M and Comedi D 2014 Enhanced optical properties and (Zn, Mg) interdiffusion in vapour transport grown ZnO/MgO core/shell nanowires *Nanotechnology* **25** 35705

[11] Grinblat G, Bern F, Barzola-Quiquia J, Tirado M, Comedi D and Esquinazi P 2014 Luminescence and electrical properties of single ZnO/MgO core/shell nanowires *Appl. Phys. Lett.* **104** 103113

[12] Zhang Y and Zhang B 2015 Photoluminescence performance enhancement of ZnO/MgO heterostructured nanowires and their applications in ultraviolet laser diodes *Phys. Chem. Chem. Phys.* **17** 13813–20

[13] Yang S, Wang L, Wang Y, Li L, Wang T and Jiang Z 2015 Identification and characteristics of ZnO/MgO core–shell nanowires *AIP Adv.* **5** 037122

[14] Gao M *et al* 2013 Synthesis and characterization of aligned ZnO/MgO core–shell nanorod arrays on ITO substrate *Appl. Phys.* B **112** 539–45

[15] Richters J-P, Voss T, Kim D S, Scholz R and Zacharias M 2008 Enhanced surface-excitonic emission in ZnO/Al_2O_3 core–shell nanowires *Nanotechnology* **19** 305202

[16] Bozyigit D, Yazdani N, Yarema M, Yarema O, Lin W M M, Volk S, Vuttivorakulchai K, Luisier M, Juranyi F and Wood V 2016 Soft surfaces of nanomaterials enable strong phonon interactions *Nature* **531** 618–22

[17] Shan W, Walukiewicz W, Ager J W, Yu K M, Yuan H B, Xin H P, Cantwell G and Song J J 2005 Nature of room temperature photoluminescence in ZnO *Appl. Phys. Lett.* **86** 1–3

[18] Marin O, Grinblat G, Gennaro A, Tirado M, Koropecki R R and Comedi D 2015 On the origin of white photoluminescence from ZnO nanocones/porous silicon heterostructures at room temperature *Superlattices Microstruct.* **79** 29–37

[19] Chen C-Y, Durán Retamal J R, Wu I-W, Lien D-H, Chen M-W, Ding Y, Chueh Y-L, Wu C-I and He J-H 2012 Probing surface band bending of surface-engineered metal oxide nanowires *ACS Nano* **6** 9366–72

[20] Chen Q, Ding H, Wu Y, Sui M, Lu W, Wang B, Su W, Cui Z and Chen L 2013 Passivation of surface states in the ZnO nanowire with thermally evaporated copper phthalocyanine for hybrid photodetectors *Nanoscale* **5** 4162–5

[21] Dzhagan V M, Valakh M Y, Raevska O E, Stroyuk O L, Kuchmiy S Y and Zahn D R T 2009 The influence of shell parameters on phonons in core–shell nanoparticles: a resonant Raman study *Nanotechnology* **20** 365704

[22] Voss T, Bekeny C, Wischmeier L, Gafsi H, Börner S, Schade W, Mofor A C, Bakin A and Waag A 2006 Influence of exciton–phonon coupling on the energy position of the near-band-edge photoluminescence of ZnO nanowires *Appl. Phys. Lett.* **89** 182107

[23] Ahn C H, Mohanta S K, Lee N E and Cho H K 2009 Enhanced exciton–phonon interactions in photoluminescence of ZnO nanopencils *Appl. Phys. Lett.* **94** 261904

[24] Wang R P, Xu G and Jin P 2004 Size dependence of electron–phonon coupling in ZnO nanowires *Phys. Rev.* B **69** 113303

[25] Jin C, Kim H, Hong C, Lee J and Lee C 2011 Luminescence properties of MgO-sheathed and annealed ZnO nanowires *Curr. Appl. Phys.* **11** S60–4

[26] Kiliç Ç and Zunger A 2002 N-type doping of oxides by hydrogen *Appl. Phys. Lett.* **81** 73–5

[27] Yan X, Fan S, Zhang X and Ren X 2015 Analysis of critical cimensions for nanowire core-multishell heterostructures *Nanoscale Res. Lett.* **10** 389–95

[28] Watanabe K, Nagata T, Wakayama Y, Sekiguchi T, Erdélyi R and Volk J 2015 Band-gap deformation potential and elasticity limit of semiconductor free-standing nanorods characterized *in situ* by scanning electron microscope-cathodoluminescence nanospectroscopy *ACS Nano* **9** 2989–3001

[29] Jones E J, Ermez S and Gradečak S 2015 Mapping of strain fields in GaAs/GaAsP core–shell nanowires with nanometer resolution *Nano Lett.* **15** 7873–9

[30] Stankevič T *et al* 2015 Strain mapping in an InGaN/GaN nanowire using a nano-focused x-ray beam *Appl. Phys. Lett.* **107** 103101

[31] Yang Q, Wu Y, Liu Y, Pan C and Wang Z L 2014 Features of the piezo-phototronic effect on optoelectronic devices based on wurtzite semiconductor nanowires *Phys. Chem. Chem. Phys.* **16** 2790–800

[32] Janotti A and Van der Walle C G 2007 Absolute deformation potentials and band alignment of wurtzite ZnO, MgO, and CdO *Phys. Rev.* B **75** 121201

[33] Plank N O V, Snaith H J, Ducati C, Bendall J S, Schmidt-Mende L and Welland M E 2008 A simple low temperature synthesis route for ZnO-MgO core–shell nanowires *Nanotechnology* **19** 465603

[34] Schleicher F *et al* 2014 Localized states in advanced dielectrics from the vantage of spin- and symmetry-polarized tunnelling across MgO *Nat. Commun.* **5** 4547

[35] Li M, Xing G, Xing G, Wu B, Wu T, Zhang X and Sum T C 2016 Origin of green emission and charge trapping dynamics in ZnO nanowires *Phys. Rev.* B **87** 115309